Nano Research 2016, 9(7): 1891–1903
DOI 10.1007/s12274-016-1081-2
Research Article
ISSN 1998-0124
CN 11-5974/O4

Inside-out Ostwald ripening: A facile process towards synthesizing anatase TiO_2 microspheres for high-efficiency dye-sensitized solar cells

Yong Ding[1,2], Xin Xia[1], Wangchao Chen[2], Linhua Hu[2] (✉), Li'e Mo[2], Yang Huang[2], and Songyuan Dai[1,2] (✉)

[1] *Beijing Key Laboratory of Novel Thin-Film Solar Cells, North China Electric Power University, Beijing 102206, China*
[2] *Key Laboratory of Novel Thin-film Solar Cells, Institute of Applied Technology, Hefei Institutes of Physical Science, Chinese Academy of Sciences, Hefei 230031, China*

Received: 18 December 2015
Revised: 17 March 2016
Accepted: 21 March 2016

KEYWORDS
Ostwald ripening, dye-sensitized solar cell, TiO_2 microsphere, hollow structure, acetylacetone

ABSTRACT

A facile inside-out Ostwald ripening route to the morphology-controlled preparation of TiO_2 microspheres is developed. Here, TiO_2 hollow microspheres (HM) and solid microspheres (SM) are prepared by adjusting the volume ratio of isopropanol (IPA) to acetylacetone (Acac) in the solvothermal process. During the formation process of HM, precipitation of solid cores, subsequent deposition of outer shells on the surface of cores, and simultaneous core dissolution and shell recrystallization are observed, which validate the inside-out Ostwald ripening mechanism. Design and optimization of the properties (pore size, surface area, and trap state) of TiO_2 microspheres are vital to the high performance of dye-sensitized solar cells (DSSCs). The optimized TiO_2 microspheres (rHM and rSM) obtained by post-processing on recrystallization, possess large pore sizes, high surface areas and reduced trap states (Ti^{3+} and oxygen vacancy), and are thus ideal materials for photovoltaic devices. The power conversion efficiency of DSSCs fabricated using rHM photoanode is 11.22%, which is significantly improved compared with the 10.54% efficiency of the rSM-based DSSC. Our work provides a strategy for synthesizing TiO_2 microspheres that simultaneously accommodate different physical properties, in terms of surface area, crystallinity, morphology, and mesoporosity.

1 Introduction

Dye-sensitized solar cells (DSSCs) have attracted extensive interest in the past twenty years and have been regarded as prospective thin-film solar cells [1, 2]. It is well known that the design of highly efficient photovoltaic devices is guided by three basic principles: (1) employing hierarchical TiO_2 nanostructures with large diameters for efficient light scattering, (2) enlarging specific surface areas and developing mesoporous

Address correspondence to Linhua Hu, solarhu@sina.com; Songyuan Dai, sydai@ipp.cas.cn

structure for sufficient dye loading, and (3) constructing continuous electron transport pathways for rapid electron collection [3]. Therefore, design and optimization of the properties of TiO_2 are crucial to the development of high-efficiency DSSCs.

Synthetic fabrication of TiO_2 hollow microspheres has been highlighted as a promising approach to meet the above-mentioned criteria [4–7]. Various methods have been developed, such as those based on sacrificial template [4], gas bubble [8], and emulsion micelles [9], to synthesize TiO_2 hollow microspheres. Those methods are advantageous in the effective and versatile preparation of hollow structures, but disadvantageous due to the high-cost and tedious synthetic procedures. Thus, it is highly desirable to explore convenient and cost-effective synthetic strategies for hollow structures. Recent research development has been steered to self-template routes based on Ostwald ripening [10], Kirkendall effect [11], and galvanic replacement reaction [12]. Among them, Ostwald ripening has been demonstrated to be a facile process to fabricate symmetric and/or asymmetric interior spaces, including core/shell spaces and multiple shell spaces. During this process, the initial tiny nanocrystals, which are located at the interior part of aggregation, dissolve and recrystallize on the large nanocrystals at the outer surface to decrease the Gibbs free energy of the system. However, the formation mechanism is not clearly understood, and synthesis of TiO_2 hollow structures with large pores, high surface areas and crystallinity remains a challenge.

In this work, we report a facile route for the simultaneous synthesis of TiO_2 hollow microspheres (HM) and solid microspheres (SM) by adjusting the volume ratio of reaction solvent in the solvothermal process. The significance of the present work is highlighted on the proposed mechanism for the formation of HM. During the fabrication of HM, we have observed the formation process of core/shell structures, consisting of three steps: precipitation of solid cores, subsequent precipitation of the outer shell on the surface of cores, and core dissolution and shell recrystallization. This observation provides direct evidence in support of the inside-out Ostwald ripening mechanism. To improve the crystallinity, pore size, and porosity of the HM and SM, these microspheres were recrystallized with ammonia in autoclave and are referred to as rHM and rSM, respectively. The optimized rHM and rSM thus obtained, possess larger pores, higher porosity, better crystallinity, and fewer trap states compared to HM and SM. At the same time, rHM shows better performance than rSM in terms of dye loading, light scattering, and electron collection efficiency, resulting in a power conversion efficiency up to 11.22% for rHM-based DSSC, which is much higher than that of rSM-based DSSC (10.54%).

2 Experimental

2.1 Synthesis of TiO_2 HM and SM

All chemicals were analytical-grade reagents and used without further purification. The TiO_2 hollow and solid microspheres were prepared via a facile template-free solvothermal reaction treatment by adjusting the volume ratio of the mixed solvent. The solution composition of titanium tetra-isopropyl (TTIP):isopropanol (IPA):acetylacetone (Acac) was varied in the range of (0.2–0.8):(0–5.0):(0–5.0). In a typical synthesis of HM, 10 mL of Acac was dissolved in 40 mL of IPA, followed by the addition of 2 mL of TTIP under vigorous stirring at ambient temperature. On the other hand, SM was synthesized by mixing 25 mL of IPA and 25 mL of Acac with 2 mL TTIP. The two resulting yellowish solutions were sealed within a Teflon-lined autoclave (100 mL) and heated at 200 ˚C for 16 h. After filtration and ethanol washing, the powders were dried at 60 ˚C for 12 h in air to remove organic components and produce the microspheres for characterization.

2.2 Synthesis of TiO_2 rHM and rSM

To prepare mesoporous titania microspheres with a highly crystalline framework, a second solvothermal treatment was performed. The as-obtained HM and SM were individually dispersed in a 40 mL ethanol and 20 mL deionized water mixture with an ammonia content of 0.5 mL. Then the resulting mixtures were stirred at ambient conditions for 30 min and transferred to a Teflon-lined autoclave (100 mL) and heated at 160 ˚C for 16 h. The white precipitates were collected and washed with water and ethanol several times. The as-obtained microspheres from HM and SM were

denoted as rHM and rSM, respectively.

2.3 Fabrication of DSSCs

In this study, TiO_2 nanocrystallines (NP, 20 nm in diameter) were synthesized following the same procedure as described in a previous report [13]. Five pastes (NP, HM, rHM, SM, and rSM) were prepared according to the procedures described in our previous work [13]. In view of the weak adhesion between TiO_2 sub-microsphere and fluorine-doped tin oxide (FTO) glass (15 $\Omega \cdot sq^{-1}$), a ~3.6-μm-thick TiO_2 nanocrystalline layer was fabricated as a bridge prior to screen-printing on the FTO glass, to link the TiO_2 sub-microspheres and the FTO glass [14]. The as-prepared five mixed pastes were repeatedly screen-printed onto the FTO glass and then sintered in air at 510 ℃ for 30 min. For comparison, commercial TiO_2 large particles (400 nm in diameter) were screen-printed on the nanocrystalline layer as the scattering layer. The thicknesses of the films were measured by a profilometer (XP-2, AMBIOS Technology, Inc., USA). The average thickness of the films was about 13.5 μm.

The five freshly prepared TiO_2 photoanodes were soaked in 0.1 M $TiCl_4$ aqueous solution and stored in a closed container at 65 ℃ for 40 min. Those films were sintered again at 450 ℃ for 30 min after washing with distilled water. Then, the five films were immersed in a 300 μM C101 dye with cheno-3a, 7a-dihydroxy-5b-cholic acid overnight. After being washed by acetonitrile and dried in air, the dye-loaded photoanodes were assembled with a Pt-modified counter-electrode and high-efficiency electrolyte composed of 30 mM I_2, 50 mM LiI, 1 M 1,3-dimethylimidazolium iodide (DMII), 0.5 M tert-butylpyridine, and 0.1 M guanidinium thiocyanate (GuSCN) in a solvent mixture of 85% acetonitrile with 15% valeronitrile by volume.

2.4 TiO_2 characterization and photovoltaic characterization

The composition and crystal structure of the products were analyzed by X-ray diffraction (XRD, MXPAHF, Mark Corp., Japan) with a scanning rate of 10 °·min^{-1} in the 2θ range from 20° to 70° and the crystallite sizes were calculated using the Scherrer equation. X-ray photoelectron spectroscopy (XPS, ESCALAB 250, Thermo Scientific) was used to determine the chemical composition of the powders by calibration of C 1s peak (284.6 eV). Electron paramagnetic resonance spectroscopy (EPR, Bruker EMX-10/12 plus) was used to examine paramagnetic species on TiO_2.

The product solution obtained after solvothermal synthesis was filtered to remove any remaining particles and then analyzed using two-dimensional liquid chromatography-mass spectrometry (2D-LC-MS, Thermo Fisher Scientific). The morphology of the microspheres was investigated by field emission scanning electron microscopy (FE-SEM, JSM-6700F, JEOL, Japan). Field emission transmission electron microscopy (FE-TEM) was performed using a JEM-2100F transmission electron microscope with accelerating voltage of 200 kV. The Brunauer–Emmett–Teller (BET) surface area and pore size distribution of the microspheres were evaluated by using a micromeritics (BELSORP-mini instrument) nitrogen adsorption/desorption apparatus. UV–vis diffuse reflection spectra and absorption spectra were obtained from a UV–vis spectrophotometer (SOLID 3700, Shimadzu Co. Ltd., Japan) to measure the diffuse reflectance of the films and the dye amounts detached from the films, respectively.

Current density/voltage (*J*–*V*) measurements were carried out on a Keithley model 2420 digital source meter controlled by Test point software under a xenon lamp (100 mW·cm^{-2}). The active area of photoanodes was 0.25 cm^2. The incident photon conversion efficiency (IPCE) of the DSSCs was determined as a function of wavelength from 300 to 800 nm (PV Measurements, Inc.). An electrochemical workstation (IM6e, Zahner, Germany) was used to perform intensity-modulated photocurrent/photovoltage spectroscopy (IMPS/IMVS) by using light emitting diodes (LED, λ = 610 nm) driven by Export (Zahner, Germany). Small amplitude was 10% or less than that of the dc component provided by the LED, and the frequency range was from 300 mHz to 3 kHz.

3 Results and discussion

As shown in Scheme 1, HM was synthesized via a simple one-step route of hydrolyzing the titania precursors in the mixed IPA/Acac solvent, where the volume ratio of IPA to Acac is 4:1. The preparation

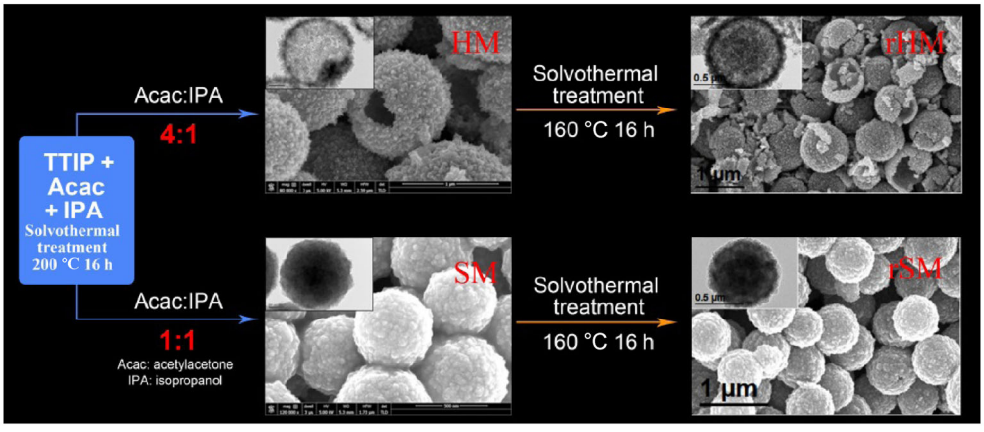

Scheme 1 Schematic illustration of the preparation of TiO_2 hollow microspheres and solid microspheres, and recrystallization process for obtaining the optimized TiO_2 hollow microspheres and solid microspheres.

method is based on the reaction between TTIP and Acac following a typical aldol condensation depicted in Scheme S1 (in the Electronic Supplementary Material (ESM)). The carbanion nucleophilically attacks the second Acac molecule to form the C–C bond. The enolate complex is obtained as well as a water molecule. The third Acac molecule provides a secondary attack to the enolate. Meanwhile, the generated water acts as the oxygen source for the formation of TiO_2 [15, 16].

The crystal structure and morphological characteristic of the HM were characterized by XRD, SEM, TEM, and N_2 absorption/desorption measurements, as shown in Fig. 1. It can be seen from the XRD pattern (Fig. 1(a)) that all the diffraction peaks of HM can be well indexed to the anatase phase of TiO_2 (JCPDS No. 21-1272) and the average crystallite size is 15.4 nm, as calculated using the Scherrer equation. From the SEM image (Fig. 1(d)), it is apparent that the HM consists of interconnected primary nanocrystals with diameter in the range of 700–1,100 nm. As shown in Fig. 1(e), the broken microsphere of the HM indicates the hollow structure in the HM. TEM images (Figs. 1(f) and 1(g)) provide further insight into the hollow structure. Each hollow microsphere is filled with a solid core with a size of about 200 nm and shell thickness of approximately 60 nm. In addition, the HM is composed of primary tapering nanorods, presenting a rough surface and mesoporous structure (Fig. 1(h)). The latter is additionally confirmed by the N_2 absorption/desorption measurement (Fig. 1(b)). In Fig. 1(b), the N_2 adsorption isotherm shows a steep H2 loop, and its specific surface area is 136.2 $m^2 \cdot g^{-1}$. A narrow pore size distribution with a sharp peak at 2.5 nm can be found in the inset (Fig. 1(c)).

To study the formation mechanism of the HM, time-dependent experiments were carried out. As shown in Fig. S1(a) (in the ESM), smooth spherical aggregations are produced at the initial state of the reaction. With the increase of reaction time to 4 h (Fig. 2(a)), sheet-like crystals are randomly deposited on the surface of these aggregations by homogeneous nucleation and growth [17]. After further reaction for 30 min, more crystals are coated on the surface of these aggregations (Fig. 2(b)). Subsequently, shells are gradually formed and consolidated (Fig. 2(c)). Compared to the sheet-like crystals of the outer shell, the inner core composed of numerous tiny particles has high surface energies due to having a higher curvature. Thus, the inner core has a strong tendency to dissolve and regrow on the outer shells [5, 18]. As the reaction progresses, the outer shell becomes more rough, indicating enhanced crystal growth (Figs. S1(b)–S1(f) in the ESM). As confirmed by the XRD patterns in Fig. S2 (see ESM), the diffraction peaks of (101) gradually become sharper and more intensive with increasing reaction time. The above observations suggest that the morphological evolution and crystallization process are different from those reported in the previously published articles, in which the hollowing process is believed to start from the core of the microspheres [10, 18].

The time-dependence of the hollow-structure

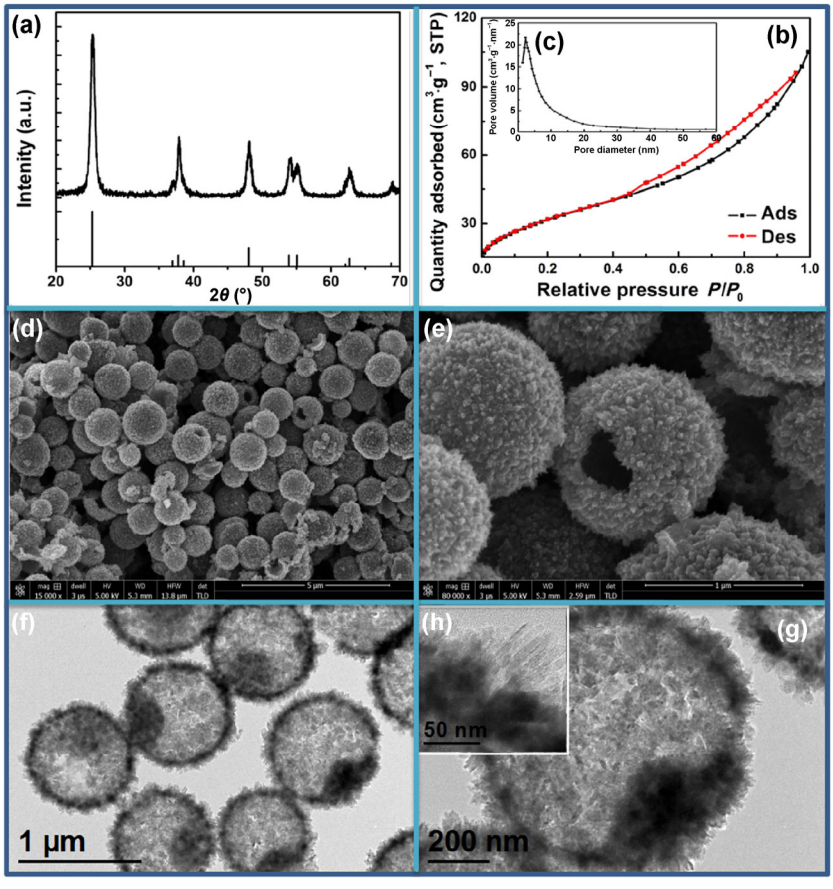

Figure 1 XRD pattern (a), N_2 adsorption/desorption isotherm (b) and the corresponding pore size distribution (c), SEM images (d) and (e), and TEM images (f)–(h) of HM.

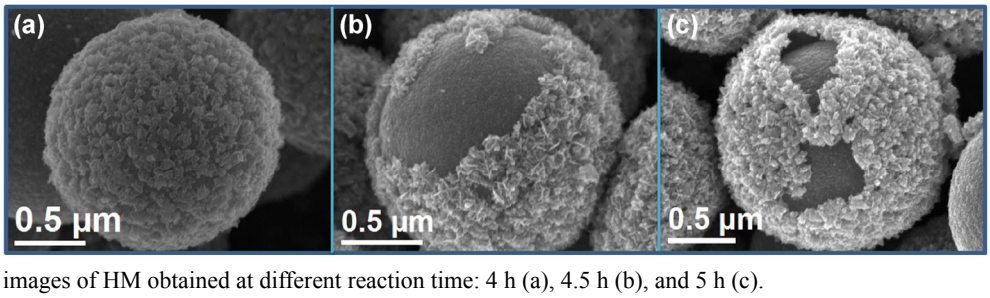

Figure 2 SEM images of HM obtained at different reaction time: 4 h (a), 4.5 h (b), and 5 h (c).

formation mechanism was further elucidated by TEM analysis, as shown in Fig. 3. The initial state of the reaction comprises solid microspheres composed of tiny primary crystals (Fig. 3(b)). It is interesting that the hollowing process begins with the region of microsphere beneath the shell, not from the center of the microsphere, indicating that the side beneath the shell is less dense or composed of smaller crystals (Fig. 3(c)). The above observations (Fig. 2(b)) indicate that the outer shell, which is larger than the side beneath the shell, is composed of sheet-like crystals. As a result, the smaller crystals in the inner cores have higher surface energies compared to those in the outer shells, which have a strong tendency to dissolve and diffuse through the shell. At this stage, the core and shell begin to separate, and interior space appears. Additionally, the inner cores are further dissolved into a smaller size, while the outer crystallites become larger on absorbing the smaller crystallites underneath, with a longer reaction time (Figs. 3(d)–3(f))

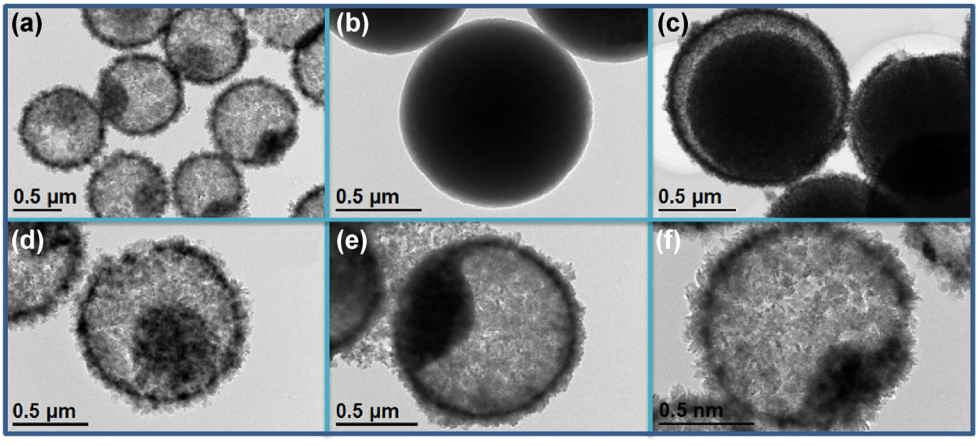

Figure 3 TEM images of HM obtained at different reaction time: 16 h (a), 3 h (b), 5 h (c), 8 h (d), 16 h (e), and 48 h (f).

[5, 19]. Therefore, it can be deduced that the formation of the TiO_2 hollow microspheres can be divided into three stages: (1) precipitation of solid cores, (2) subsequent deposition of the outer shell on the surface of cores, and (3) core dissolution and shell recrystallization, which follows the typical asymmetric inside-out Ostwald ripening in the formation of hollow structure [20–22].

By tuning the volume ratio of IPA to Acac from 4 to 1 in the synthesis route of HM, SM can be prepared. Acac acts as a morphological controller to the self-assembly of primary nanocrystals and forms uniform microspheres. The crystal structure of SM was examined by XRD patterns (Fig. 4(a)), similar to the case of HM. The SEM images in Figs. 4(d) and 4(e) show that all of SM consists of uniform microspheres with a diameter of ~700 nm and a smooth surface. As shown in Figs. 4(f)–4(h), SM is a solid structure composed of interconnected tiny nanocrystals. As revealed by N_2 adsorption analysis (Fig. 4(b)), SM exhibits type-IV isotherm plots with an H2 hysteresis loop [21], indicating a typical mesoporous structure. The surface area of SM is as high as 114.3 $m^2 \cdot g^{-1}$, and small mesopores are also observed (Fig. 4(c)).

Time-dependent study of the formation mechanism of SM was carried out as was done for HM. As shown in Fig. S3 (see ESM), it is clear that the SM entirely consists of solid microspheres during the whole process. Therefore, the formation mechanism of SM is different from that of HM. At the initial stage of reaction, primary particles of titania are formed by stepwise hydrolysis of titanium tetra-isopropyl using the generated water molecule, as discussed above. The higher the water concentration produced in the reaction solution, the faster is the hydrolysis rate, and the more are the primary particles obtained [23]. The high density of primary particles makes them assemble together to form solid spherical aggregates incompactly, which is consistent with the observation in Fig. S3 (in the ESM) [5]. According to a previous report by Zeng et al., the loosely packed aggregations serve as starting points for the subsequent recrystallization process because of the majority of primary crystals in the surrounding solution [10, 18]. Thus, the above results on the formation mechanism of HM and SM demonstrate that the primary crystal concentrations play a key role in the crystal nucleation and growth, and final morphology [24, 25].

To synthesize TiO_2 microspheres with large pores and high crystallinity, the microspheres (HM and SM) were placed in autoclave again, to recrystallize with ammonia. Under solvothermal condition, ammonia works as a reagent to reduce the solubility of hydroxide precipitate in ethanol, which conversely increases the solubility of the precipitate and enhances the particle growth [26, 27]. As indicated in Fig. S4 (in the ESM), the crystallinity of the optimized rHM and rSM are increased. In addition, they have a similar diameter and morphology, except for a small fraction of dispersed shell in rHM (Fig. 5(a)). TEM images of a single microsphere (Figs. 5(g) and 5(j)) show that the nanosized building units are similar in shape and size (18 nm).

These units abut against each other and form a mesoporous structure. High-resolution TEM (HRTEM) image of rHM in Fig. 5(e) clearly shows the lattice of (200) and (020) planes with a right angle [28]. The angle reflected in the corresponding fast Fourier transform (FFT) image (Fig. 5(f)) is also 90°, which is in accordance with the theoretical value for the angle between (200) and (020) planes. The HRTEM image

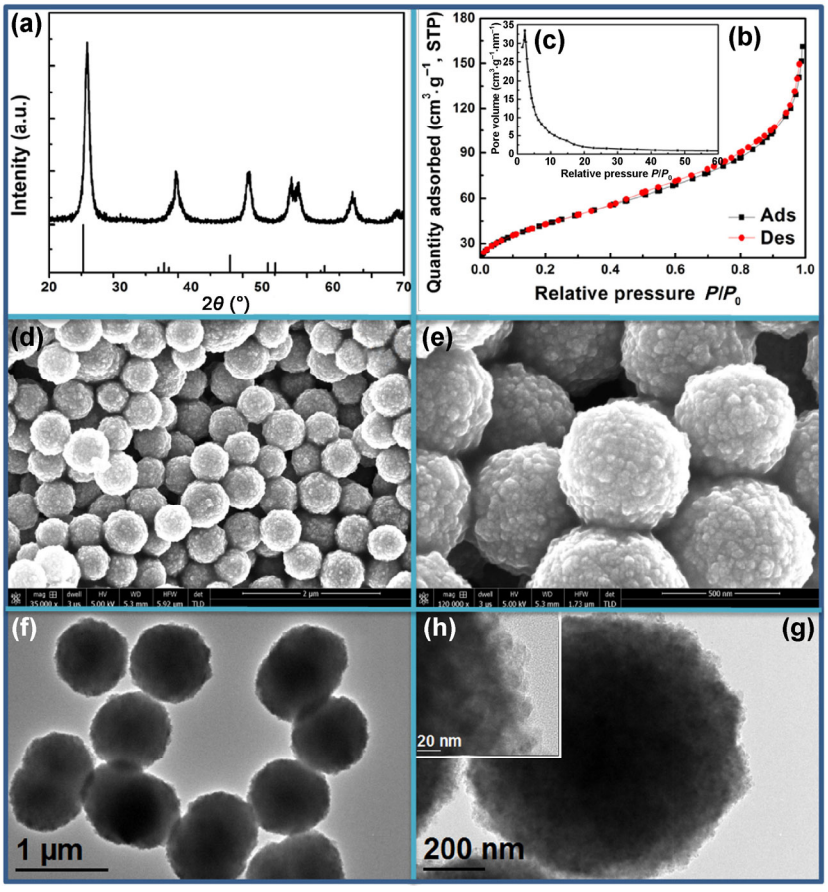

Figure 4 XRD pattern (a), N_2 adsorption/desorption isotherm (b) and the corresponding pore size distribution (c), SEM images (d) and (e), and TEM images (f)–(h) of SM.

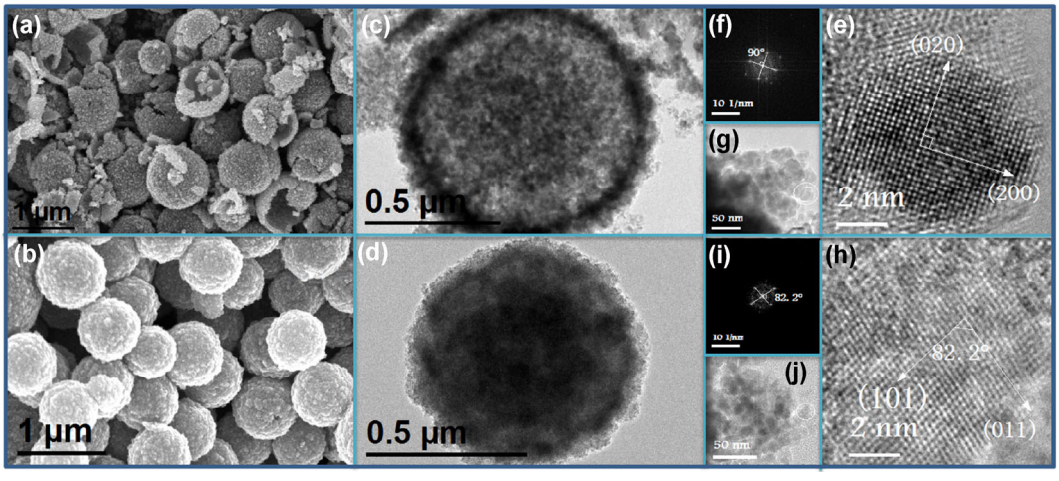

Figure 5 SEM image (a), TEM image (c), HRTEM image (e), corresponding FFT pattern (f), and enlarged TEM image (g) of rHM; SEM image (b), TEM image (d), HRTEM image (h), corresponding FFT pattern (i), and enlarged TEM image (j) of rSM.

of rSM (Fig. 5(h)) reveals that the lattice of (101) and (011) planes has a dihedral angle of 82° [29].

The porous structure of rHM and rSM were further confirmed by N_2 adsorption/desorption analysis, as shown in Fig. S5 (in the ESM). Unlike HM and SM, the N_2 adsorption isotherms of rHM and rSM microspheres show a steep H1 loop [30]. The hysteresis loops shift to a higher relative pressure from 0.8 to 1.0, which is closely associated with the increase of pore sizes. As shown in Fig. S5(b) (in the ESM) and summarized in Table S1 (see ESM), the optimized rHM and rSM show an increase in pore size but a slight decrease in specific surface areas. These variations are concurrent with the fact that the crystal sizes increased after the recrystallization process (Fig. S4, ESM).

As shown in Fig. 6(a), XPS was used to investigate the electronic structure of TiO_2 microspheres [31, 32]. Two peaks at the binding energies of 458.7 ± 0.2 and 464.4 ± 0.2 eV are observed for Ti $2p_{3/2}$ and Ti $2p_{1/2}$, respectively. It is interesting to note that the Ti $2p_{3/2}$ peaks of rHM shifts to a higher energy than those of HM, indicating the presence of a small amount of Ti^{3+} trap states. In this case, the total Ti $2p_{3/2}$ peak can be fitted into two Gaussian peaks with peak energy at

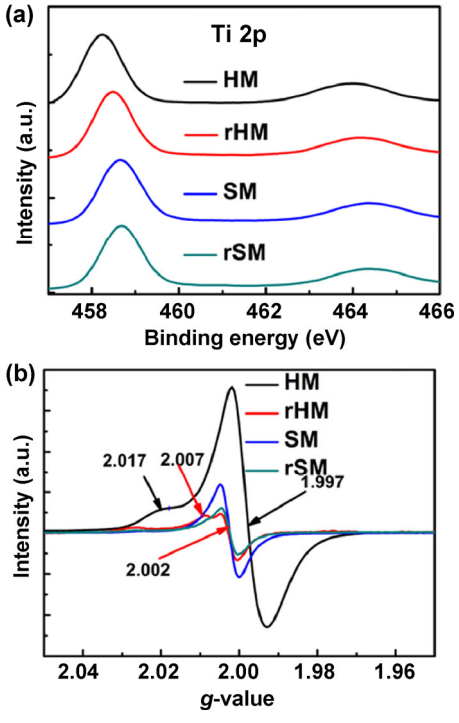

Figure 6 Ti 2p XPS spectra (a) and EPR spectra at 1.8 K (b) for HM, rHM, SM, and rSM samples.

458.2 and 457.8 eV, which are attributed to the $2p_{1/2}$ core level of Ti^{4+} and Ti^{3+}, respectively (Fig. S6(a), ESM) [33]. These quantitative analyses of the XPS data (Table S2, ESM) are used in the calculation of the $Ti^{3+}/(Ti^{3+} + Ti^{4+})$ atomic ratio. It is found that nearly 11.04% of Ti in HM is present in the form of Ti^{3+}. From the XPS data, it can be seen that the Ti^{3+} concentration decreases after recrystallization.

This modification can be further established using the EPR spectra (Fig. 6(b)). The EPR spectra recorded at 1.8 K was used to confirm the presence of paramagnetic Ti^{3+} centers and oxygen vacancy centers, which has also been previously reported by Ke et al. in case of anatase TiO_2 [34, 35]. As shown in Fig. 6(b), HM gives rise to a prominent signal at g = 1.997, which unambiguously demonstrates the presence of Ti^{3+} centers in the bulk. In addition, a weak signal at g = 2.017 might originate from surface oxygen vacancy centers. In contrast, no evident signal at g = 2.017 is observed for rHM. The existence of weak signals at g = 2.002 and g = 2.007 is attributed to surface oxygen vacancy centers [33, 35]. However, there is little difference between SM and rSM in terms of XPS and EPR results, compared with the case of HM and rHM. This is probably because SM undergoes a minor change in the second solvothermal treatment to produce rSM [5]. In general, the optimized rHM and rSM have better crystallinity and lesser trap states than HM and SM, respectively, which contribute to reducing the electron recombination at the dyed-TiO_2/electrolyte interface.

In order to explore the potential of microspheres for photovoltaic devices, we have prepared photoanodes using a screen-printing technique. In general, this is realized by employing a bilayer structure design of photoanode: a transparent layer to link the substrate with microspheres, and a top layer composed of microspheres to trap the incident light [14, 27].

To confirm the light scattering effect of TiO_2 microsphere-based photoanodes, UV–vis diffused reflection was employed (Fig. 7). The NP-based photoanode composed of nanocrystallines and commercial large particles has the worst light scattering effect. In addition, due to the comparable size of SM and rSM to the wavelength of visible light, strong scattering over 70% in the entire wavelength range of 400–800 nm is

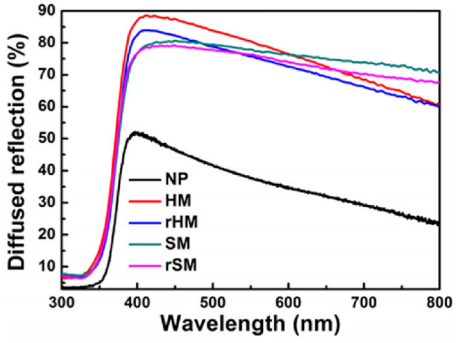

Figure 7 Diffused reflection spectra of the five photoanodes.

expected from the Mie theory [36–38]. The reflectance of HM is higher than that of SM in the wavelength range of 400 to 600 nm due to multiple reflection and scattering between shells and cores, as illustrated in Scheme 2. However, a distinctly rapid decline in reflectance in the wavelength range of 600 to 800 nm is observed for HM films because of the existence of broken microspheres, resulting in more of a Rayleigh-type scattering ($I_{scat} \propto \lambda^{-4}$) [39]. Compared with the HM and SM films, the optimized rHM and rSM are slightly inferior in light scattering capability.

The photocurrent density–voltage (J–V) curves of photoanodes prepared with the four kinds of microspheres and NP are shown in Fig. 8(a). Table 1 summarizes the photovoltaic performance of the DSSCs employing different types of photoanodes. The fill factor (FF) values are similar to each other but the open-circuit voltage (V_{oc}) is slightly varied. The increased V_{oc} of rHM and rSM is attributed to the improved crystallinity and reduced trap states. Except for the photoanode composed of SM, the overall energy-conversion efficiency (η) of DSSCs is higher for HM, rHM, and rSM than that for NP. The higher η results from superior light scattering owing to the higher short-circuit current density (J_{sc}) [37]. To further illustrate this, the IPCE spectra were recorded and are shown in Fig. 8(b). Compared to the NP-based DSSCs, the rHM-, HM-, and rSM-based DSSCs exhibit higher IPCE at both short and long wavelengths.

Interestingly, the DSSC based on rHM shows the highest η of 11.22%, which is much better than that of the DSSCs based on HM (10.64%) and rSM (10.54%). The improvement in η is mostly related to the higher J_{sc} of the former than the latter two (19.85 mA·cm^{-2}

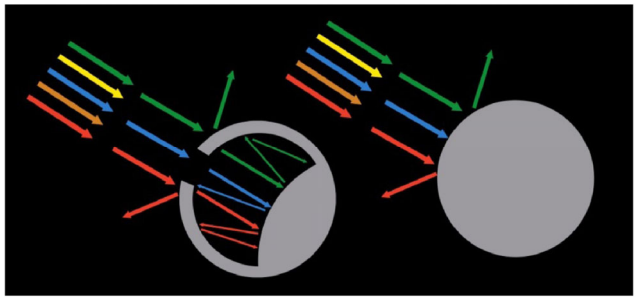

Scheme 2 Model of multiple reflection and scattering in the hollow microspheres and solid microspheres.

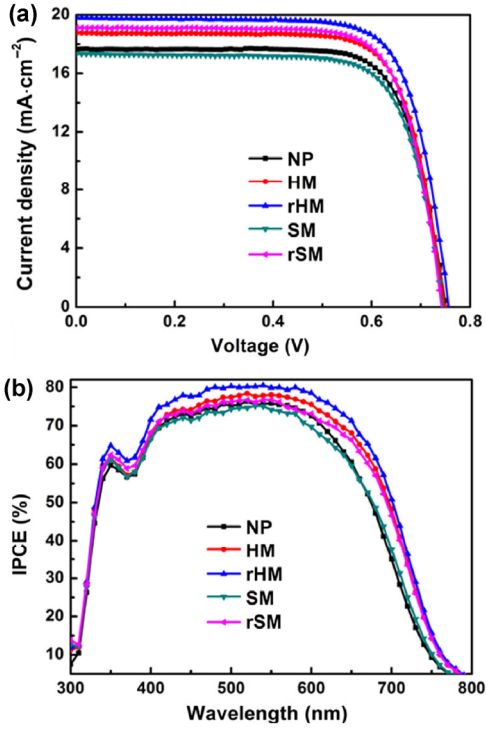

Figure 8 J–V curves of DSSCs fabricated from the five photoanodes, recorded at 100 mW·cm^{-2} (a) and corresponding IPCE spectra (b).

Table 1 Summary of photovoltaic characteristics of DSSCs based on different types of photoanodes with the corresponding dye loading capacity

Cell	V_{oc} (V)	J_{sc} (mA·cm^{-2})	FF	η (%)	Dye loading ($\times 10^{-7}$ mol·cm^{-2})
NP	0.750	17.71	0.749	9.94	1.643
HM	0.742	19.17	0.748	10.64	1.597
rHM	0.756	19.85	0.747	11.22	1.794
SM	0.744	17.41	0.741	9.59	1.619
rSM	0.748	18.79	0.749	10.54	1.748

versus 19.17 and 18.79 mA·cm^{-2}, Table 1). Generally, J_{sc} can be approximated by the following equations

$$J_{sc} = q \times \mathrm{IPCE}(\lambda) \times I_0 \quad (1)$$

$$\mathrm{IPCE}(\lambda) = \mathrm{LHE}(\lambda) \times \phi_{inj} \times \eta_c \quad (2)$$

where q is the elementary charge, I_0 is the light intensity, LHE(λ) is the light-harvesting efficiency of a cell, ϕ_{inj} is the charge-injection efficiency, and η_c is the electron collection efficiency [40]. First, ϕ_{inj} can be ignored, which is generally very close to 100% for ruthenium dye (the C101 dye used in this work) sensitized on microspheres. LHE(λ) is mainly determined by Beer's law expressed using the equation, LHE(λ)=1 − $10^{-\Gamma\times\sigma(\lambda)}$, where Γ is the surface coverage of the sensitizer and σ is the molar cross section of C101 dye (for Z907 dye, $\sigma = 1.22 \times 10^7$ cm^2·mol^{-1} at 540 nm) [40, 41]. The dye loading capacity of the five different photoanodes is listed in Table 1. The amount of dye adsorbed on the microspheres is disproportionate to their surface area, because the dye loading capacity is dependent on three aspects: surface areas, pore sizes and exposed facets [42–44]. Although the HM and SM photoanodes have high surface areas, their small pore size would restrict the dye loading capacity. On the other hand, the rHM film has the highest dye loading capacity resulting from its hollow structure, large pore size and exposed (200)-facet. Accordingly, $\mathrm{LHE}_{(540\ nm)}$ is calculated to be 99.0%, 98.8%, 99.3%, 98.9%, and 99.3% for the NP, HM, rHM, SM, and rSM-based photoanode, respectively. Such a minor difference indicates that there should be other factors affecting J_{sc}. Hence, we investigate the effect of η_c on J_{sc}.

η_c is determined by the kinetic competition between electron transport (τ_d) and recombination (τ_n), according to the relation $\eta_c = 1 - \tau_d/\tau_n$ [45]. τ_d and τ_n are functions of light intensity and are obtained from the IMPS/IMVS measurements (Fig. S7, ESM). As shown in Fig. S7(a) (see ESM), τ_d of the rHM- and rSM-based photoanodes is shorter than that of HM- and SM-based photoanodes, respectively. Electron transport in the rHM-based film is slightly faster than that in rSM-based film, mainly due to the fragments from cracked hollow microspheres, as confirmed by SEM images in Fig. 5(a). Those fragments are prone to filling into the holes between the adjacent microspheres and are sintered together with the microspheres to form a closely linked network, which would promote electron transport [46, 47]. As shown in Fig. S7(b) (see ESM), τ_n of the five kinds of photoanodes is found in the order of rHM > rSM > NP > SM > HM-based photoanode at 96 mW·cm^{-2}. From the above sequence, it appears that the optimized rHM and rSM with reduced trapping sites (the concentrations of trap sites are nearly proportional to their contents of Ti^{3+} centers, as listed in Table S2 (in the ESM)), always correspond to long τ_n. Besides, the formation of closely linked network mentioned above can explain the higher τ_n of rHM-based DSSC than that of rSM-based DSSC. Therefore, the larger the difference between τ_d and τ_n, the higher η_c is achieved (Fig. S8, ESM). By comprehensive analysis of LHE(λ) and η_c values for the five different photoanodes, the IPCE values are found to be in the sequence of rHM > HM > rSM > NP > SM-based photoanode. The higher IPCE of HM-based photoanode than that of rSM-based photoanode might be because of the stronger scattering ability of the former in the wavelength region of 400–600 nm to compensate the lower η_c, as indicated by the diffused reflectance spectra in Fig. 7.

4 Conclusions

In summary, we have demonstrated the possibility of producing HM and SM with integrated features simultaneously by adjusting the ratio of IPA to Acac in the solvothermal process. On the basis of time-dependent experiment, the formation of HM has been established to involve the inside-out Ostwald ripening mechanism, including three stages: (1) precipitation of solid cores, (2) subsequent deposition of the outer shell on the surface of cores, and (3) core dissolution and shell recrystallization. Further recrystallization paves the way for achieving mesoporous microspheres (rHM and rSM) with enhanced crystallinity and reduced trap states, which improve the dye adsorption, accelerate electron transport, and restrain electron recombination simultaneously. The optimized rHM-based photoanode is expected to multi-reflect incident light and adsorb dye molecules in the interior hollow microspheres, which make it superior to the rSM-based photoanode. Therefore, the

performance of DSSC based on rHM photoanode is optimized to obtain η = 11.22%, which is superior to that, η = 10.54%, of a rSM-type DSSC. Thus, the facile TiO_2 microsphere-synthesizing technique reported here is promising for fabricating high-performance photovoltaic devices.

Acknowledgements

We acknowledge the Steady High Magnetic Field Facility in High Magnetic Field Laboratory, Chinese Academy of Sciences for the EPR measurement. This work was supported by the National Natural Science Foundation of China (Nos. 21173228 and 61204075), and the National High-Tech Research and Development Program of China (No. 2015AA050602).

Electronic Supplementary Material: Supplementary material (schematic illustration of the formation mechanism, supporting images, XRD, XPS, and BET measurements, and electron transport and recombination characteristics) is available in the online version of this article at http://dx.doi.org/10.1007/s12274-016-1081-2.

References

[1] O'Regan, B.; Grätzel, M. A low-cost, high-efficiency solar cell based on dye-sensitized colloidal TiO_2 films. *Nature* **1991**, *353*, 737–740.

[2] Grätzel, M. All surface and no bulk. *Nature* **1991**, *349*, 740–741.

[3] Sauvage, F.; Chen, D. H.; Comte, P.; Huang, F. Z.; Heiniger, L. P.; Cheng, Y. B.; Caruso, R. A.; Graetzel, M. Dye-sensitized solar cells employing a single film of mesoporous TiO_2 beads achieve power conversion efficiencies over 10%. *ACS Nano* **2010**, *4*, 4420–4425.

[4] Hwang, S. H.; Yun, J.; Jang, J. Multi-shell porous TiO_2 hollow nanoparticles for enhanced light harvesting in dye-sensitized solar cells. *Adv. Funct. Mater.* **2014**, *24*, 7619–7626.

[5] Lou, X. W.; Archer, L. A.; Yang, Z. C. Hollow micro-/nanostructures: Synthesis and applications. *Adv. Mater.* **2008**, *20*, 3987–4019.

[6] Wu, X.; Lu, G. Q.; Wang, L. Z. Shell-in-shell TiO_2 hollow spheres synthesized by one-pot hydrothermal method for dye-sensitized solar cell application. *Energy Environ. Sci.* **2011**, *4*, 3565–3572.

[7] Xi, J. T.; Zhang, Q. F.; Xie, S. H.; Yodyingyong, S.; Park, K.; Sun, Y. M.; Li, J. Y.; Cao, G. Z. Fabrication of TiO_2 aggregates by electrospraying and their application in dye-sensitized solar cells. *Nanosci. Nanotech. Let.* **2011**, *3*, 690–696.

[8] Li, X. X.; Xiong, Y. J.; Li, Z. Q.; Xie, Y. Large-scale fabrication of TiO_2 hierarchical hollow spheres. *Inorg. Chem.* **2006**, *45*, 3493–3495.

[9] Li, W. J.; Coppens, M. O. Synthesis and characterization of stable hollow Ti-silica microspheres with a mesoporous shell. *Chem. Mater.* **2005**, *17*, 2241–2246.

[10] Yang, H. G.; Zeng, H. C. Preparation of hollow anatase TiO_2 nanospheres via Ostwald ripening. *J. Phys. Chem. B* **2004**, *108*, 3492–3495.

[11] Yin, Y. D.; Rioux, R. M.; Erdonmez, C. K.; Hughes, S.; Somorjai, G. A.; Alivisatos, A. P. Formation of hollow nanocrystals through the nanoscale Kirkendall effect. *Science* **2004**, *304*, 711–714.

[12] Oh, M. H.; Yu, T.; Yu, S. H.; Lim, B.; Ko, K. T.; Willinger, M. G.; Seo, D. H.; Kim, B. H.; Cho, M. G.; Park, J. H. et al. Galvanic replacement reactions in metal oxide nanocrystals. *Science* **2013**, *340*, 964–968.

[13] Hu, L. H.; Dai, S. Y.; Weng, J.; Xiao, S. F.; Sui, Y. F.; Huang, Y.; Chen, S. H.; Kong, F. T.; Pan, X.; Liang, L. Y. et al. Microstructure design of nanoporous TiO_2 photoelectrodes for dye-sensitized solar cell modules. *J. Phys. Chem. B* **2007**, *111*, 358–362.

[14] Ding, Y.; Mo, L.-E.; Tao, L.; Ma, Y.-M.; Hu, L.-H.; Huang, Y.; Fang, X.-Q.; Yao, J.-X.; Xi, X.-W.; Dai, S.-Y. TiO_2 nanocrystalline layer as a bridge linking TiO_2 sub-microspheres layer and substrates for high-efficiency dye-sensitized solar cells. *J. Power Sources* **2014**, *272*, 1046–1052.

[15] Liu, B.; Liu, L.-M.; Lang, X.-F.; Wang, H.-Y.; Lou, X. W.; Aydil, E. S. Doping high-surface-area mesoporous TiO_2 microspheres with carbonate for visible light hydrogen production. *Energy Environ. Sci.* **2014**, *7*, 2592–2597.

[16] Garnweitner, G.; Antonietti, M.; Niederberger, M. Nonaqueous synthesis of crystalline anatase nanoparticles in simple ketones and aldehydes as oxygen-supplying agents. *Chem. Commun.* **2005**, 397–399.

[17] Yu, J. G.; Liu, W.; Yu, H. G. A one-pot approach to hierarchically nanoporous titania hollow microspheres with high photocatalytic activity. *Cryst. Growth Des.* **2008**, *8*, 930–934.

[18] Liu, B.; Zeng, H. C. Symmetric and asymmetric Ostwald ripening in the fabrication of homogeneous core-shell semiconductors. *Small* **2005**, *1*, 566–571.

[19] Zeng, H. C. Ostwald ripening: A synthetic approach for hollow nanomaterials. *Curr. Nanosci.* **2007**, *3*, 177–181.

[20] Lou, X. W.; Wang, Y.; Yuan, C. L.; Lee, J. Y.; Archer, L. A. Template-free synthesis of SnO_2 hollow nanostructures with high lithium storage capacity. *Adv. Mater.* **2006**, *18*, 2325–2329.

[21] Wang, Y.; Zhu, Q. S.; Zhang, H. G. Fabrication of β-$Ni(OH)_2$ and NiO hollow spheres by a facile template-free process. *Chem. Commun.* **2005**, 5231–5233.

[22] Zhao, Y. B.; Pan, F.; Li, H.; Zhao, D. X.; Liu, L.; Xu, G. Q.; Chen, W. Uniform mesoporous anatase–brookite biphase TiO_2 hollow spheres with high crystallinity via Ostwald ripening. *J. Phys. Chem. C* **2013**, *117*, 21718–21723.

[23] Widoniak, J.; Eiden-Assmann, S.; Maret, G. Synthesis and characterisation of monodisperse zirconia particles. *Eur. J. Inorg. Chem.* **2005**, 3149–3155.

[24] Wu, W.; Zhang, S. F.; Zhou, J.; Xiao, X. H.; Ren, F.; Jiang, C. Z. Controlled synthesis of monodisperse sub-100 nm hollow SnO_2 nanospheres: A template- and surfactant-free solution-phase route, the growth mechanism, optical properties, and application as a photocatalyst. *Chem.—Eur. J.* **2011**, *17*, 9708–9719.

[25] Peng, Z. A.; Peng, X. G. Mechanisms of the shape evolution of CdSe nanocrystals. *J. Am. Chem. Soc.* **2001**, *123*, 1389–1395.

[26] Sugimoto, T.; Kojima, T. Formation mechanism of amorphous TiO_2 spheres in organic solvents. 1. Roles of ammonia. *J. Phys. Chem. C* **2008**, *112*, 18760–18771.

[27] Ding, Y.; Zhou, L.; Mo, L. E.; Jiang, L.; Hu, L. H.; Li, Z. Q.; Chen, S. H.; Dai, S. Y. TiO_2 microspheres with controllable surface area and porosity for enhanced light harvesting and electrolyte diffusion in dye-sensitized solar cells. *Adv. Funct. Mater.* **2015**, *25*, 5946–5953.

[28] Yang, H. G.; Sun, C. H.; Qiao, S. Z.; Zou, J.; Liu, G.; Smith, S. C.; Cheng, H. M.; Lu, G. Q. Anatase TiO_2 single crystals with a large percentage of reactive facets. *Nature* **2008**, *453*, 638–641.

[29] Shang, S. Q; Jiao, X. L.; Chen, D. R. Template-free fabrication of TiO_2 hollow spheres and their photocatalytic properties. *ACS Appl. Mater. Interfaces* **2012**, *4*, 860–865.

[30] Pan, J. H.; Wang, X. Z.; Huang, Q. Z.; Shen, C.; Koh, Z. Y.; Wang, Q.; Engel, A.; Bahnemann, D. W. Large-scale synthesis of urchin-like mesoporous TiO_2 hollow spheres by targeted etching and their photoelectrochemical properties. *Adv. Funct. Mater.* **2014**, *24*, 95–104.

[31] Wang, S. B.; Pan, L.; Song, J. J.; Mi, W. B.; Zou, J. J.; Wang, L.; Zhang, X. W. Titanium-defected undoped anatase TiO_2 with p-type conductivity, room-temperature ferromagnetism, and remarkable photocatalytic performance. *J. Am. Chem. Soc.* **2015**, *137*, 2975–2983.

[32] Singh, J.; Gusain, A.; Saxena, V.; Chauhan, A. K.; Veerender, P.; Koiry, S. P.; Jha, P.; Jain, A.; Aswal, D. K.; Gupta, S. K. XPS, UV–Vis, FTIR, and EXAFS studies to investigate the binding mechanism of N719 dye onto oxalic acid treated TiO_2 and its implication on photovoltaic properties. *J. Phys. Chem. C* **2013**, *117*, 21096–21104.

[33] Pan, S. S.; Lu, W.; Zhao, Y. H.; Tong, W.; Li, M.; Jin, L. M.; Choi, J. Y.; Qi, F.; Chen, S. G.; Fei, L. F.; Yu, S. F. Self-doped rutile titania with high performance for direct and ultrafast assay of H_2O_2. *ACS Appl. Mater. Interfaces* **2013**, *5*, 12784–12788.

[34] Kumar, C. P.; Gopal, N. O.; Wang, T. C.; Wong, M. S.; Ke, S. C. EPR investigation of TiO_2 nanoparticles with temperature-dependent properties. *J. Phys. Chem. B* **2006**, *110*, 5223–5229.

[35] Ke, S. C.; Wang, T. C.; Wong, M. S.; Gopal, N. O. Low temperature kinetics and energetics of the electron and hole traps in irradiated TiO_2 nanoparticles as revealed by EPR spectroscopy. *J. Phys. Chem. B* **2006**, *110*, 11628–11634.

[36] Ferber, J.; Luther, J. Computer simulations of light scattering and absorption in dye-sensitized solar cells. *Sol. Energ. Mat. Sol. C.* **1998**, *54*, 265–275.

[37] Zhang, H. M.; Yu, H.; Han, Y. H.; Liu, P. R.; Zhang, S. Q.; Wang, P.; Cheng, Y. B.; Zhao, H. J. Rutile TiO_2 microspheres with exposed nano-acicular single crystals for dye-sensitized solar cells. *Nano Res.* **2011**, *4*, 938–947.

[38] Zhang, Q. F.; Myers, D.; Lan, J. L.; Jenekhe, S. A.; Cao, G. Z. Applications of light scattering in dye-sensitized solar cells. *Phys. Chem. Chem. Phys.* **2012**, *14*, 14982–14998.

[39] Heiniger, L.-P.; Giordano, F.; Moehl, T.; Grätzel, M. Mesoporous TiO_2 beads offer improved mass transport for cobalt-based redox couples leading to high efficiency dye-sensitized solar cells. *Adv. Energy Mater.* **2014**, *4*, 1400168.

[40] Kang, T. S.; Smith, A. P.; Taylor, B. E.; Durstock, M. F. Fabrication of highly-ordered TiO_2 nanotube arrays and their use in dye-sensitized solar cells. *Nano Lett.* **2009**, *9*, 601–606.

[41] Zhang, W. J.; Xie, Y.; Xiong, D. H.; Zeng, X. W.; Li, Z. H.; Wang, M. K.; Cheng, Y. B.; Chen, W.; Yan, K. Y.; Yang, S. H. TiO_2 nanorods: A facile size- and shape-tunable synthesis and effective improvement of charge collection kinetics for dye-sensitized solar cells. *ACS Appl. Mater. Interfaces* **2014**, *6*, 9698–9704.

[42] Li, C. H.; Koenigsmann, C.; Ding, W. D.; Rudshteyn, B.; Yang, K. R.; Regan, K. P.; Konezny, S. J.; Batista, V. S.; Brudvig, G. W.; Schmuttenmaer, C. A. et al. Facet-dependent photoelectrochemical performance of TiO_2 nanostructures: An experimental and computational study. *J. Am. Chem. Soc.* **2015**, *137*, 1520–1529.

[43] Wu, X.; Chen, Z. G.; Lu, G. Q.; Wang, L. Z. Nanosized anatase TiO_2 single crystals with tunable exposed (001) facets for enhanced energy conversion efficiency of dye-sensitized solar cells. *Adv. Funct. Mater.* **2011**, *21*, 4167–4172.

[44] Chen, D. H.; Huang, F. Z.; Cheng, Y.-B.; Caruso, R. A. Mesoporous anatase TiO_2 beads with high surface areas and controllable pore sizes: A superior candidate for high-performance dye-sensitized solar cells. *Adv. Mater.* **2009**, *21*, 2206–2210.

[45] Oekermann, T.; Zhang, D. S.; Yoshida, T.; Minoura, H. Electron transport and back reaction in nanocrystalline TiO_2 films prepared by hydrothermal crystallization. *J. Phys. Chem. B* **2004**, *108*, 2227–2235.

[46] Ding, Y.; Ma, Y. M.; Tao, L.; Hu, L. H.; Li, G.; Jiang, L.; Li, Z. Q.; Mo, L. E.; Yao, J. X.; Dai, S. Y. Continuous electron transport pathways constructed in TiO_2 sub-microsphere films for high-performance dye-sensitized solar cells. *RSC Adv.* **2015**, *5*, 17493–17500.

[47] Thapa, A.; Zai, J. T.; Elbohy, H.; Poudel, P.; Adhikari, N.; Qian, X. F.; Qiao, Q. Q. TiO_2 coated urchin-like SnO_2 microspheres for efficient dye-sensitized solar cells. *Nano Res.* **2014**, *7*, 1154–1163.